Progress In Electromagnetics Research C, Vol. 171, 280–287, 2026

(Received 2 June 2026, Accepted 12 June 2026, Scheduled 22 June 2026)

Elliptical Skewed Halbach-Type Magnet for Cogging Torque Minimization of Axial Flux PMSM with Distributed Winding Stator

Zhongan Yu, Long Chen*, Zihao Deng, Feng Zhang, Fangrong Wang, and Zhiguo Zhu

School of Electrical Engineering and Automation, Jiangxi University of Science and Technology, Ganzhou 341000, Jiangxi, China

ABSTRACT: To address the inherent significant average torque degradation in conventional Axial Flux Permanent Magnet (AFPM) machines when the pole-shift method is employed for cogging torque suppression, this paper proposes a novel Elliptical-Cut Rotating Compensated Halbach Pole Axial Flux Permanent Magnet (EC-RCHP AFPM) machine. The proposed machine suppresses cogging torque via elliptically cut rotating poles and compensates for the induced torque loss by introducing dedicated compensating Halbach auxiliary poles. First, the rotor topology of the proposed machine is presented, and an equivalent surface current model is established to elucidate its operating mechanism. Second, sensitivity analysis and response surface methodology are adopted to investigate the correlation between design parameters and performance responses, and the optimal parameter combination is obtained under given constraints. Finally, the electromagnetic characteristics of the proposed machine are comprehensively analyzed through three-dimensional finite element analysis (3D-FEA). The results demonstrate that compared with the conventional machine, the EC-RCHP AFPM machine reduces cogging torque by 54.9%, increases average output torque by 1.8%, and lowers torque ripple to 6.12%, effectively resolving the fundamental trade-off between cogging torque suppression and torque output retention.

1. INTRODUCTION

In recent years, the global energy crisis and environmental pollution have become increasingly severe. As one of the primary sectors responsible for energy consumption and carbon emissions, the transportation industry's green transition has emerged as a critical initiative for nations worldwide to achieve their carbon neutrality targets. Benefiting from their inherent zero-emission and high energy efficiency, new energy vehicles (NEVs) are gradually replacing conventional internal combustion engine vehicles and have become the mainstream development direction of the global automotive industry [1]. With the continuous advancement of NEV technology, drive motors are subject to increasingly stringent requirements for high torque density, high efficiency, and lightweight design to satisfy the ever-rising vehicle performance standards [2, 3].

Among numerous motor topologies, axial-flux permanent magnet (AFPM) machines exhibit superior torque and power densities, shorter axial lengths, and more compact structures than traditional radial-flux permanent magnet machines. They have been successfully applied in a variety of high-end NEVs and demonstrate broad application prospects [4]. Nevertheless, AFPM machines inherently suffer from considerable torque ripple caused by unbalanced axial magnetic force, which exacerbates motor vibration and deteriorates vehicle ride comfort and control precision [5–7]. Consequently, how to effectively suppress cogging torque while preserving the high torque density and high efficiency of AFPM machines has become a prominent research hotspot and technical challenge in the field of AFPM machine design.

To mitigate cogging torque in permanent magnet machines, researchers have conducted extensive investigations and proposed various effective suppression strategies, mainly including pole-slot combination optimization [8], skewed pole and slot techniques [9], and stator slot opening optimization [10]. Among these strategies, the pole-shift method has attracted widespread attention owing to its advantages of simple structure, no requirement for stator modification, and ease of engineering implementation. Ref. [11] proposed and designed a novel stator semi-skewed slot method utilizing an inclined laser cutting process, which reduced design costs and improved motor operational efficiency. Ref. [12] presented a novel rotor skewed pole design method based on a multi-objective optimization algorithm to suppress specific vibrations in modular dual-three-phase permanent magnet synchronous machines. Ref. [13] developed a segmented model to address the adverse effects caused by the uneven axial distribution of vibration modes, which significantly enhanced the evaluation accuracy of rotor skewed pole schemes. However, the conventional pole-shift method inevitably leads to a substantial reduction in the average output torque of the machine while suppressing cogging torque, which severely limits its application in high-performance drive scenarios [14, 15].

To boost the output torque of permanent magnet machines, Halbach permanent magnet arrays have been extensively employed [16] due to their remarkable unilateral magnetic focus-

---

* Corresponding author: Long Chen (18370031053@163.com).

doi:10.2528/PIERC26060205

Published by THE ELECTROMAGNETIC ACADEMY

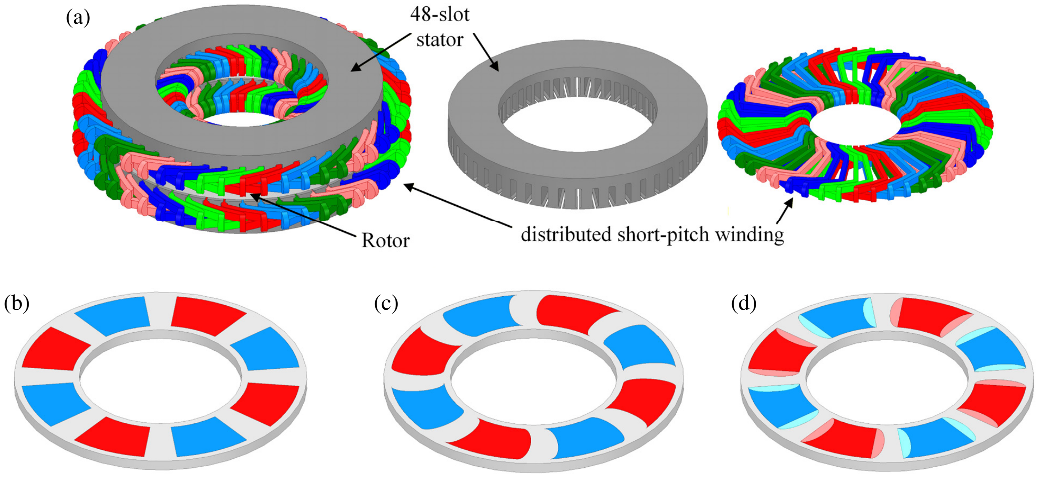

FIGURE 1. Machine topologies. (a) Stator structure of three machines, (b) CAFPM rotor, (c) EC-RP AFPM rotor, and (d) EC-RCHP AFPM rotor.

ing effect achieved through the special arrangement of permanent magnets. Ref. [17] proposed a combined Halbach array suitable for YASA-type AFPM machines, which effectively improved the torque density and permanent magnet utilization of the machine. Ref. [18] designed and analyzed a magnetic gear reducer adopting a Halbach permanent magnet array, and the proposed novel magnetic gear structure significantly enhanced the output torque density.

Aiming at the inherent contradiction between torque loss and cogging torque suppression caused by the conventional pole-shift method, this paper proposes a novel AFPM machine based on elliptically cut rotating Halbach poles. Compared with the conventional machine, the proposed machine reduces torque ripple while moderately improving the output torque. The main contributions of this paper are summarized as follows:

1) An Elliptical Cut Rotating Pole Axial Flux Permanent Magnet (EC-RP AFPM) machine is proposed. Compared with the conventional AFPM machine, the proposed EC-RP AFPM machine achieves cogging torque reduction but suffers from a concomitant decrease in output torque.

2) Based on the EC-RP AFPM machine, an Elliptical Cut Rotating Compensated Halbach Pole Axial Flux Permanent Magnet (EC-RCHP AFPM) machine is further proposed. The mechanism of torque enhancement and ripple reduction of the proposed machine is elucidated through equivalent surface current analysis.

3) A genetic algorithm-based optimization method for improving the output torque of the EC-RCHP AFPM machine is developed and validated. This method integrates finite element (FE) modeling with the equivalent surface current model to optimize the rotor structure of the EC-RCHP AFPM machine, thereby achieving output torque improvement.

The remainder of this paper is organized as follows. Section 2 elaborates on the deficiencies of the conventional AFPM machine and EC-RP AFPM machine, based on which the EC-RCHP AFPM machine is proposed. Meanwhile, the operating principle of the EC-RCHP AFPM machine is clarified through equivalent surface current analysis. Section 3 conducts multi-objective optimization for the topology of the EC-RCHP AFPM machine and compares its comprehensive performance on the basis of output torque improvement. Section 4 verifies the effectiveness and accuracy of the proposed machine through finite element analysis. Section 5 concludes the whole paper.

2. MACHINE TOPOLOGY AND OPERATING PRINCIPLES

2.1. Machine Topology

Taking the conventional axial-flux permanent magnet (CAFPM) machine as the baseline, this paper designs an EC-RP AFPM machine to suppress the cogging torque of AFPM machines. However, the EC-RP AFPM machine inevitably leads to a moderate decrease in output torque. Therefore, by introducing rotating-compensated elliptical Halbach permanent magnets, this paper further proposes an EC-RCHP AFPM machine, as shown in Figure 1.

Figure 1(a) presents the stator structures of all three machines, which share identical winding configurations with an 8-pole 48-slot design. The complete machine topology is illustrated, adopting a double-stator single-rotor axial structure with two stators on the upper and lower sides and a rotor disc in the middle. This stator employs a distributed short-pitch winding design with a winding pitch $y = 4$ and a pole pitch $\tau = 6$, satisfying the short-pitch winding design criterion. Each phase consists of 32 coils with 7 turns per coil, resulting in a total of 224 series turns per phase. This winding structure effectively suppresses cogging torque and high-order harmonic contents, thereby improving the steady-state operational performance and electromagnetic compatibility of the machine.

Figures 1(b)–(d) show the differences in the rotor structures of the CAFPM, EC-RP AFPM, and EC-RCHP AFPM machines. Figure 2 depicts the step-by-step evolution process from the CAFPM rotor to the EC-RP AFPM and EC-RCHP AFPM rotors. The CAFPM machine adopts an interior permanent magnet (IPM) arrangement. By applying an elliptical pole topology shift to its permanent magnets, the permanent magnetic field is offset, yielding the EC-RP AFPM rotor. This elliptical beveled structure is custom-designed to combine

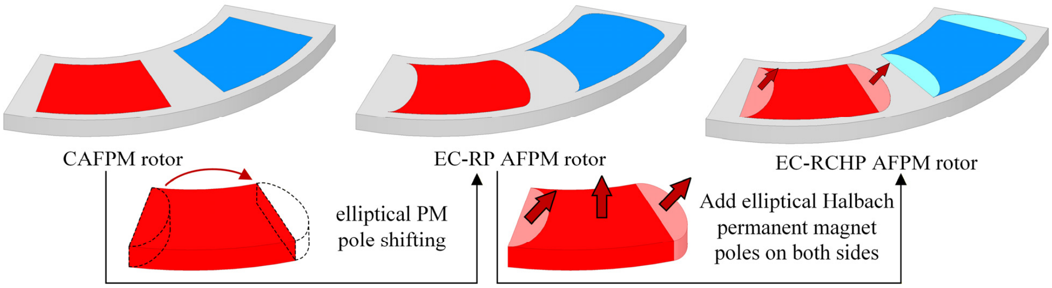

FIGURE 2. The gradual evolution of the CAFPM rotor structure into the EC-RP AFPM and EC-RCHP AFPM rotor structures.

the characteristics of the disc-type rotor and the circumferential magnetic field of an axial-flux motor. Its smooth, curved contour adapts to the annular rotor structure, forming a continuous and uniform equivalent surface current. On this basis, elliptical Halbach auxiliary poles are symmetrically added on both sides of the main permanent magnets, and a Halbach array structure with alternating magnetization directions is introduced, thus forming the final EC-RCHP AFPM machine.

2.2. Equivalent Surface Current Analysis

For the cogging torque suppression of the EC-RCHP AFPM machine, the cogging torque is mathematically defined as the negative partial derivative of the magnetic coenergy W with respect to the rotor position α [19]:

$$T_{cog} = -\frac{\partial W}{\partial \alpha} \tag{1}$$

In the EC-RCHP AFPM machine, the magnetic flux propagates along the axial direction. Neglecting the variation of magnetic coenergy in permanent magnets and assuming that the magnetic coenergy is solely determined by the air-gap magnetic field, the magnetic coenergy can be expressed as:

$$W = \frac{1}{2\mu_0} \int_V \Lambda^2(\theta, r, z) B^2(\theta, r, z, \alpha) dV \tag{2}$$

In traditional axial-flux permanent magnet motors, the main poles are typically magnetized axially. For the proposed EC-RCHP AFPM machine, this paper adopts the equivalent surface current method to analytically calculate the spatial air-gap magnetic field produced by Halbach permanent magnet arrays with different magnetization directions. Based on *Ampère*'s molecular current hypothesis, this method equates the magnetic field of a rectangular permanent magnet to the field collectively generated by four sets of line currents on its four edges [20, 21], as shown in Figure 3.

Considering the inherent characteristics of AFPM machines that the air-gap magnetic field exhibits periodic circumferential distribution and a small radial magnetic field gradient, this paper adopts a multi-segment 2D unfolding method to facilitate the analysis. The machine is radially divided into multiple concentric rings, each of which is unfolded into a linear machine at its average radius with radial edge effects neglected. The 3D air-gap magnetic field is obtained by radially superimposing the 2D magnetic fields of each individual cross-section, which significantly reduces analytical complexity while ensuring computational accuracy. Based on the fundamental principles of modeling using the equivalent surface current method, the axes a-b and c-d in Figure 3 are selected as the local reference axes for the permanent magnet.

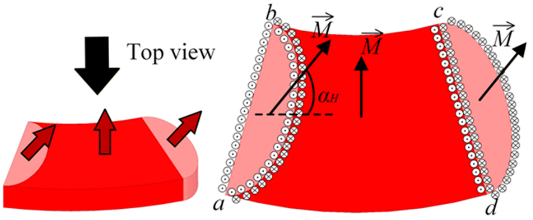

FIGURE 3. Equivalent surface current method model of the EC-RCHP AFPM machine.

The expression for the outer surface current is given by:

$$\vec{K} = \vec{M} \times \vec{n} \tag{3}$$

Here, $\vec{M}$ represents the magnetization of the permanent magnet, and $\vec{n}$ represents the unit normal vector to the surface.

The normal vector to the left arc ab in Region I: $\vec{n}_{I\text{-}ab} = (-\cos\theta, -\sin\theta)$, where θ is the polar angle of the arc, $\theta \in [-\pi/2, \pi/2]$, and the parametric equation of the arc is $x = -L/2 + R\cos\theta$, $y = R\sin\theta$.

The surface currents along the four edges of Region I are:

$$\begin{aligned} K_{\text{I-}ab}(\theta) &= -M\cos\theta \\ K_{\text{I-}cd} &= M \end{aligned} \tag{4}$$

Similarly, the surface current along the four sides of Region II is:

$$\begin{aligned} K_{\text{II-}ab} &= -M\cos\alpha \\ K_{\text{II-}ab}(\theta) &= M\cos(\alpha+\theta) \end{aligned} \tag{5}$$

The surface currents along the four sides of Region III are:

$$\begin{aligned} K_{\text{III-}cd} &= -M\cos\alpha \\ K_{\text{III-}cd}(\theta) &= M\cos(\alpha+\theta) \end{aligned} \tag{6}$$

Sum the surface currents along the coincident edges:

$$\begin{aligned} K_{ab}(\theta) &= M\cos(\alpha+\theta) - M\cos\theta \\ K_{cd} &= M - M\cos\theta \end{aligned} \tag{7}$$

A positive value of K indicates that the current direction is out of the page, while a negative value indicates that it is into the page.

Based on the *Biot-Savart* law, the analytical expression for the magnetic flux density produced by a finite-length uniform planar current sheet at any arbitrary point in space can be derived. This formula constitutes the core fundamental basis of the equivalent surface current method in the electrical machine field:

$$\begin{cases} B_x = \frac{\mu_0 K}{4\pi}\sin\beta\cdot\ln\left(\frac{r_0^2}{r_1^2}\right) - \frac{\mu_0 K}{2\pi}\cos\beta\cdot\mathrm{sign}(l)\cdot\varphi \\ B_y = \frac{\mu_0 K}{4\pi}\cos\beta\cdot\ln\left(\frac{r_1^2}{r_0^2}\right) - \frac{\mu_0 K}{2\pi}\sin\beta\cdot\mathrm{sign}(l)\cdot\varphi \end{cases} \tag{8}$$

Here, β is the angle between the current-carrying line segment and the positive x-axis; r_0 and r_1 are the distances from the field point to the start and end points of the line segment, respectively; l is the perpendicular distance from the field point to the current-carrying line segment; and φ is the angle subtended by the line segment at the field point.

The magnetic field generated in space by the equivalent current in the cd side is expressed as:

$$\begin{cases} B_{x\text{-}cd} = \frac{\mu_0 M(1-\cos\theta)}{4\pi}\cdot\ln\left(\frac{(x-L/2)^2+(y+R)^2}{(x-L/2)^2+(y-R)^2}\right) \\ B_{y\text{-}cd} = -\frac{\mu_0 M(1-\cos\theta)}{2\pi}\cdot\mathrm{sign}(x-L/2) \\ \quad\cdot\left(\arctan\frac{y+R}{x-L/2} - \arctan\frac{y-R}{x-L/2}\right) \end{cases} \tag{9}$$

The magnetic field generated in space by the equivalent current in the ab side is expressed as:

$$\begin{cases} B_{x\text{-}ab} = \frac{-\mu_0 M\cos\alpha}{4\pi}\cdot\ln\left(\frac{(x+L/2+R)^2+(y+R)^2}{(x+L/2+R)^2+(y-R)^2}\right) \\ B_{y\text{-}ab} = \frac{\mu_0 M\cos\alpha}{2\pi}\cdot\mathrm{sign}(x+L/2+R) \\ \quad\cdot\left(\arctan\frac{y+R}{x+L/2+R} - \arctan\frac{y-R}{x+L/2+R}\right) \end{cases} \tag{10}$$

For a curved surface with a nonuniform surface current distribution, the magnetic field does not possess an elementary analytical solution and is therefore expressed in the form of a definite integral. For a semicircular arc-shaped surface centered at (x_c, y_c) with radius R and surface current density $K(\theta)$, the magnetic field is given by:

$$\begin{cases} B_x(\theta) = \frac{\mu_0 R}{2\pi}\cdot\int_{-\pi/2}^{\pi/2} \\ \qquad \frac{K(\theta)(y-y_c-R\sin\theta)}{(x-x_c-R\sin\theta)^2+(y-y_c-R\sin\theta)^2}\,d\theta \\ B_y(\theta) = \frac{\mu_0 R}{2\pi}\cdot\int_{-\pi/2}^{\pi/2} \\ \qquad \frac{K(\theta)(x_c-x+R\cos\theta)}{(x-x_c-R\sin\theta)^2+(y-y_c-R\sin\theta)^2}\,d\theta \end{cases} \tag{11}$$

The magnetic field generated in space by the arc ab in Region I is:

$$\begin{cases} B_{x\text{-I-}ab}(\theta) = \frac{-\mu_0 MR}{2\pi}\cdot\int_{-\pi/2}^{\pi/2} \\ \qquad \frac{\cos\theta(y-R\sin\theta)}{(x+L/2+R-R\cos\theta)^2+(y-R\sin\theta)^2}\,d\theta \\ B_{y\text{-I-}ab}(\theta) = \frac{-\mu_0 RM}{2\pi}\cdot\int_{-\pi/2}^{\pi/2} \\ \qquad \frac{\cos\theta(R\cos\theta-L/2-R-x)}{(x+L/2+R-R\cos\theta)^2+(y-R\sin\theta)^2}\,d\theta \end{cases} \tag{12}$$

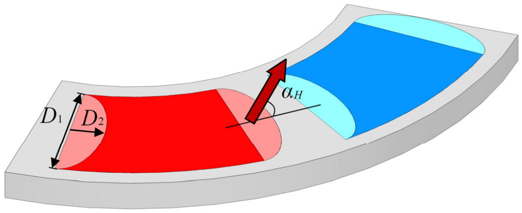

FIGURE 4. Key parameters of the EC-RCHP AFPM machine.

The magnetic field generated by the arc ab in Region II is:

$$\begin{cases} B_{x\text{-II-}ab}(\theta) = \frac{\mu_0 MR}{2\pi}\cdot\int_{-\pi/2}^{\pi/2} \\ \qquad \frac{\cos(\alpha+\theta)(y-R\sin\theta)}{(x+L/2+R-R\cos\theta)^2+(y-R\sin\theta)^2}\,d\theta \\ B_{y\text{-II-}ab}(\theta) = \frac{\mu_0 RM}{2\pi}\cdot\int_{-\pi/2}^{\pi/2} \\ \qquad \frac{\cos(\alpha+\theta)(R\cos\theta-L/2-R-x)}{(x+L/2+R-R\cos\theta)^2+(y-R\sin\theta)^2}\,d\theta \end{cases} \tag{13}$$

The magnetic field generated in space by the Region III arc-shaped cd is:

$$\begin{cases} B_{x\text{-III-}cd}(\theta) = \frac{\mu_0 MR}{2\pi}\cdot\int_{-\pi/2}^{\pi/2} \\ \qquad \frac{\cos(\alpha+\theta)(y-R\sin\theta)}{(x-L/2-R\cos\theta)^2+(y-R\sin\theta)^2}\,d\theta \\ B_{y\text{-III-}cd}(\theta) = \frac{\mu_0 RM}{2\pi}\cdot\int_{-\pi/2}^{\pi/2} \\ \qquad \frac{\cos(\alpha+\theta)(R\cos\theta+L/2-x)}{(x-L/2-R\cos\theta)^2+(y-R\sin\theta)^2}\,d\theta \end{cases} \tag{14}$$

To calculate the magnetic field generated by the aforementioned arc, the Simpson's 1/3 numerical integration rule is adopted, which achieves a numerical error on the order of 10^{-4}. The integration step size is set to $d\theta = \pi/N$, and for each discrete polar angle $\theta_i = -\pi/2 + i d\theta$ $(i = 0, 1, \ldots, N)$.

$$\text{Simpson's weight: } \omega_i = \begin{cases} 1, & i = 0 \text{ or } N \\ 4, & i = \text{odd} \\ 2, & i = \text{even} \end{cases} \tag{15}$$

Based on the above numerical integration method for computational simplification, the simplified expression for the magnetic field generated by arc ab in Region I is given by:

$$\begin{cases} B_{x\text{-I-}ab}(\theta) = \frac{d\theta}{3}\sum_{i=0}^{N}\left(\omega_i\cdot\frac{-\mu_0 MR}{2\pi}\right. \\ \qquad \left.\cdot\frac{\cos\theta_i\cdot(y-R\sin\theta_i)}{[x+L/2+R(1-\cos\theta_i)]^2+(y-R\sin\theta_i)^2}\right) \\ B_{y\text{-I-}ab}(\theta) = \frac{d\theta}{3}\sum_{i=0}^{N}\left(\omega_i\cdot\frac{-\mu_0 MR}{2\pi}\right. \\ \qquad \left.\cdot\frac{\cos\theta_i\cdot[R(\cos\theta_i-1)-x-L/2]}{[x+L/2+R(1-\cos\theta_i)]^2+(y-R\sin\theta_i)^2}\right) \end{cases} \tag{16}$$

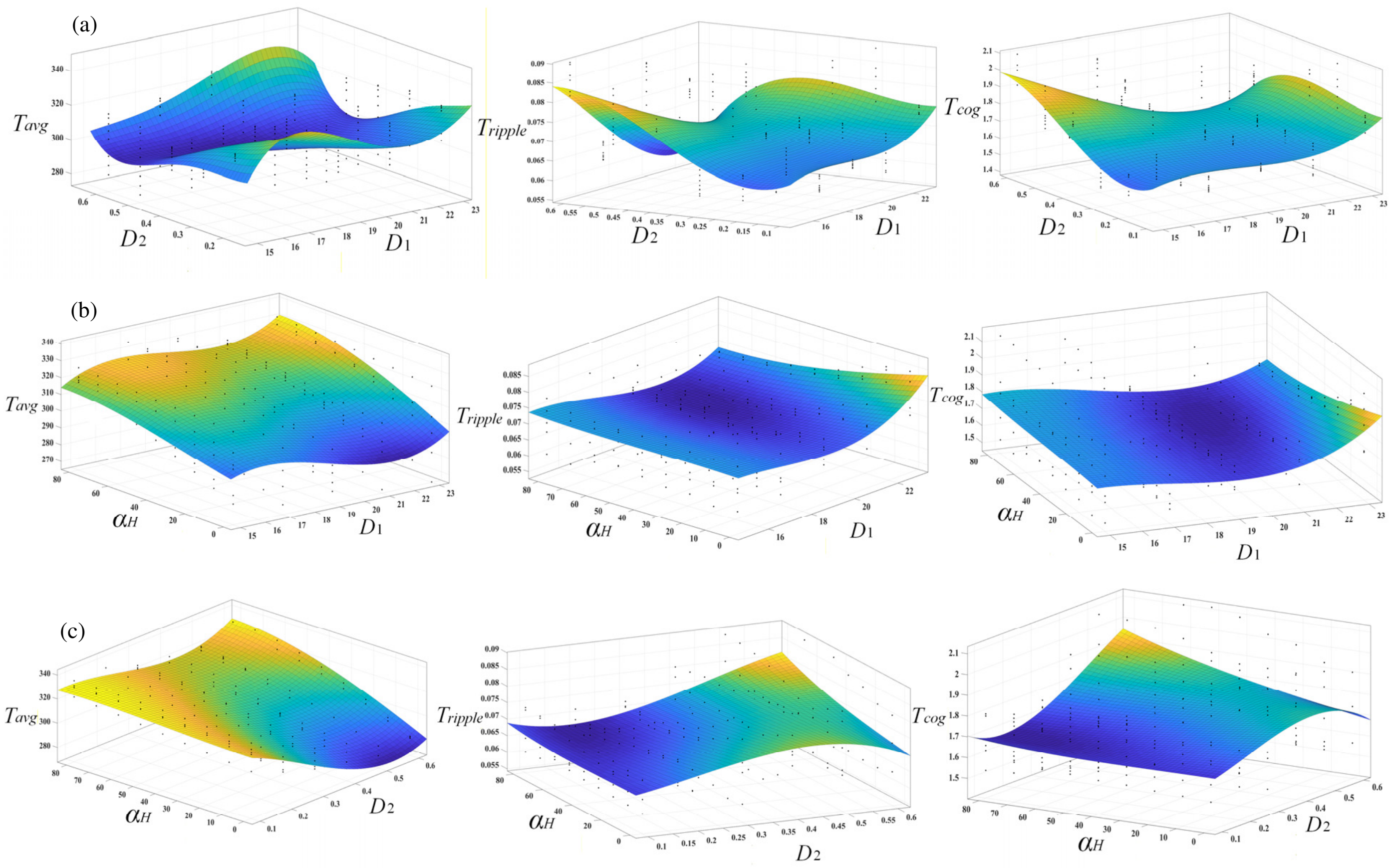

FIGURE 5. Response surface analysis of key parameters for the EC-RCHP AFPM machine: (a) response surface analysis of average torque, (b) response surface analysis of torque ripple, and (c) response surface analysis of cogging torque.

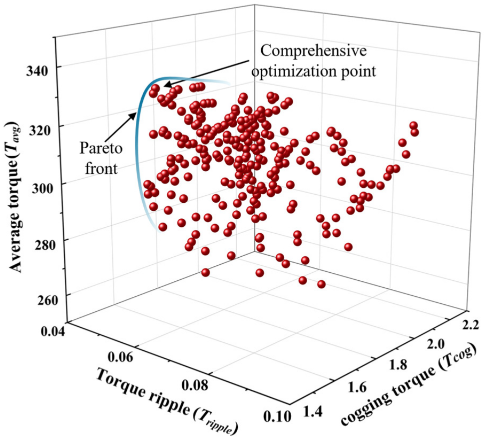

FIGURE 6. Multi-objective optimization analysis of the EC-RCHP AFPM machine.

The magnetic field generated by the curved Region II ab in space can be calculated as follows:

$$\begin{cases} B_{x\text{-II-}ab}(\theta) = \frac{d\theta}{3}\sum_{i=0}^{N}\left(\omega_i\cdot\frac{\mu_0 MR}{2\pi}\right. \\ \qquad\left.\cdot\frac{\cos(\alpha+\theta_i)\cdot(y-R\sin\theta_i)}{[x+L/2+R(1-\cos\theta_i)]^2+(y-R\sin\theta_i)^2}\right) \\ B_{y\text{-II-}ab}(\theta) = \frac{d\theta}{3}\sum_{i=0}^{N}\left(\omega_i\cdot\frac{\mu_0 MR}{2\pi}\right. \\ \qquad\left.\cdot\frac{\cos(\alpha+\theta_i)\cdot[R(\cos\theta_i-1)-x-L/2]}{[x+L/2+R(1-\cos\theta_i)]^2+(y-R\sin\theta_i)^2}\right) \end{cases} \tag{17}$$

The simplified calculation of the magnetic field generated in space by the Region III arc-shaped cd yields:

$$\begin{cases} B_{x\text{-III-}cd}(\theta) = \frac{d\theta}{3}\sum_{i=0}^{N}\left(\omega_i\cdot\frac{\mu_0 MR}{2\pi}\right. \\ \qquad\left.\cdot\frac{\cos(\alpha+\theta_i)\cdot(y-R\sin\theta_i)}{(x-L/2-R\cos\theta_i)^2+(y-R\sin\theta_i)^2}\right) \\ B_{y\text{-III-}cd}(\theta) = \frac{d\theta}{3}\sum_{i=0}^{N}\left(\omega_i\cdot\frac{\mu_0 MR}{2\pi}\right. \\ \qquad\left.\cdot\frac{\cos(\alpha+\theta_i)\cdot(R\cos\theta_i-x+L/2)}{(x-L/2-R\cos\theta_i)^2+(y-R\sin\theta_i)^2}\right) \end{cases} \tag{18}$$

The total 2D magnetic field components B_x, 2D and B_y, 2D are obtained by superimposing the magnetic fields generated by each edge in the x and y directions, respectively. The 3D air-gap magnetic field is then derived by periodically extending the 2D magnetic field of each slice along the circumferential direction and averaging the results:

$$\begin{cases} B_x = \frac{1}{Ns}\sum_{i=1}^{Ns}\sum_{n=0}^{2p-1} B_{x,2D}(x+n\tau(r_i),y,r_i) \\ B_y = \frac{1}{Ns}\sum_{i=1}^{Ns}\sum_{n=0}^{2p-1} B_{y,2D}(x+n\tau(r_i),y,r_i) \end{cases} \tag{19}$$

Here, the radial center position of each slice is r_i, and the corresponding pole pitch is $\tau(r_i)$. Substituting the derived 3D air-gap magnetic field equations into the magnetic coenergy Equation (2) demonstrates that the proposed elliptical Halbach pole-

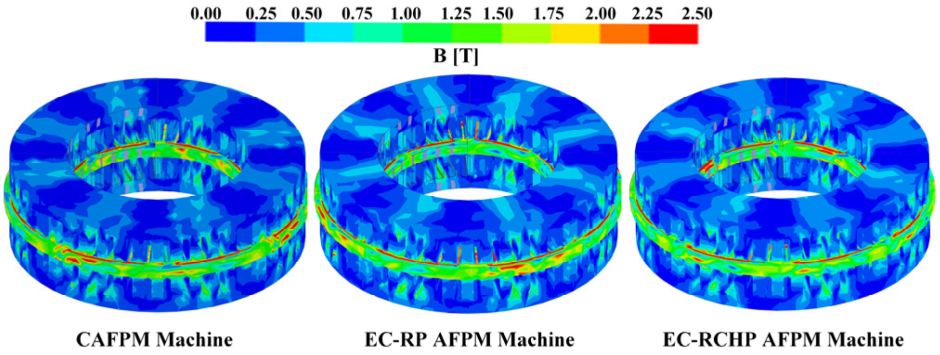

FIGURE 7. Magnetic field distribution in an open-circuit air gap.

shifted structure can suppress cogging torque and moderately improve the output torque.

3. MULTI-OBJECTIVE OPTIMIZATION DESIGN

To comprehensively investigate the performance characteristics of the proposed EC-RCHP AFPM machine in suppressing cogging torque while enhancing output torque, analytical results of the proposed machine obtained via the equivalent surface current method demonstrate that the rotor topology and permanent magnet dimensions should be prioritized for optimization to achieve optimal performance. Figure 4 presents the key design parameters of the EC-RCHP AFPM machine. D_1 is the major axis of the ellipse, D_2 the curvature of the ellipse, and a_H the Halbach magnetization angle. In addition, given that the EC-RCHP AFPM machine is required to exhibit high torque and low torque ripple characteristics, the average torque (T_{avg}), torque ripple (T_{ripple}), and cogging torque (T_{cog}) are selected as the optimization objectives.

Figure 5 presents the parametric response surface analysis of key design parameters of the proposed EC-RCHP AFPM machine with respect to average torque, torque ripple, and cogging torque. By analyzing these response surfaces, correlations between design parameters and response variables can be established, and response variables can be predicted within specified ranges. The analysis reveals that increasing α_H significantly enhances the average torque and reduces the torque ripple, but causes a sharp deterioration in cogging torque. The stator inner diameter D_1 and elliptical curvature D_2 each have distinct optimal ranges for all three performance metrics, and they exhibit strong parameter interactions with α_H. Finally, a multi-objective optimization is performed using the genetic algorithm (GA) to obtain the optimal parameter combination under the given constraints, as shown in Figure 6.

4. ELECTROMAGNETIC PERFORMANCE ANALYSIS AND COMPARISON

All three-dimensional finite element models of the AFPM motors in this paper were created and solved using ANSYS Maxwell 2022. Since edge magnetic leakage is prone to occur on the outer surface of axial flux motors, the outermost air domain of the three motor models in this paper has been set to a zero-vector magnetic potential boundary.

4.1. Air-Gap Magnetic Flux Density Characteristic Analysis

Figure 7 presents the open-circuit air-gap magnetic field distributions of the CAFPM, EC-RP AFPM, and EC-RCHP AFPM machines, respectively. Comparison of the magnetic field intensity distributions of the three machines reveals that the CAFPM machine exhibits a relatively uniform air-gap magnetic field distribution but low overall intensity; the EC-RP AFPM machine shows an increased air-gap magnetic field strength with a distinct magnetic field enhancement region at the salient pole rotor positions; and the EC-RCHP AFPM machine achieves the highest air-gap magnetic field strength and the most concentrated magnetic field distribution, demonstrating that the elliptically cut rotating-compensated Halbach poles possess a superior magnetic focusing effect.

To further quantitatively analyze the distribution characteristics of the air-gap magnetic field, Figure 8 compares the air-gap magnetic flux density waveforms of the three machines. It is observed that compared with the CAFPM machine, the air-gap magnetic flux density waveforms of the EC-RP AFPM and EC-RCHP AFPM machines exhibit a significant phase shift due to the magnetic field offset design.

4.2. Back-EMF Characteristic Analysis

Figure 9 presents a comparison of the open-circuit back-EMF (electromotive force) waveforms and their Fourier decomposition results for the three machine types at rated speed. As can be seen from Figure 9(a), the fundamental peak value of the back-EMF of the EC-RCHP AFPM machine is significantly higher than those of the CAFPM and EC-RP AFPM machines.

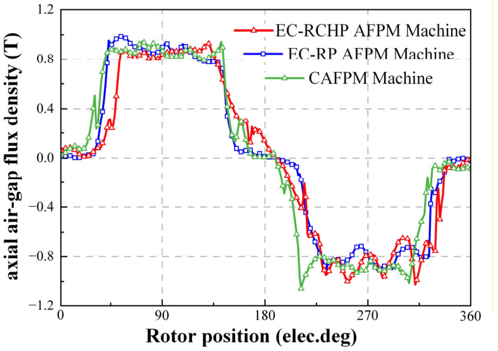

FIGURE 8. Magnetic flux density in an open-circuit air gap.

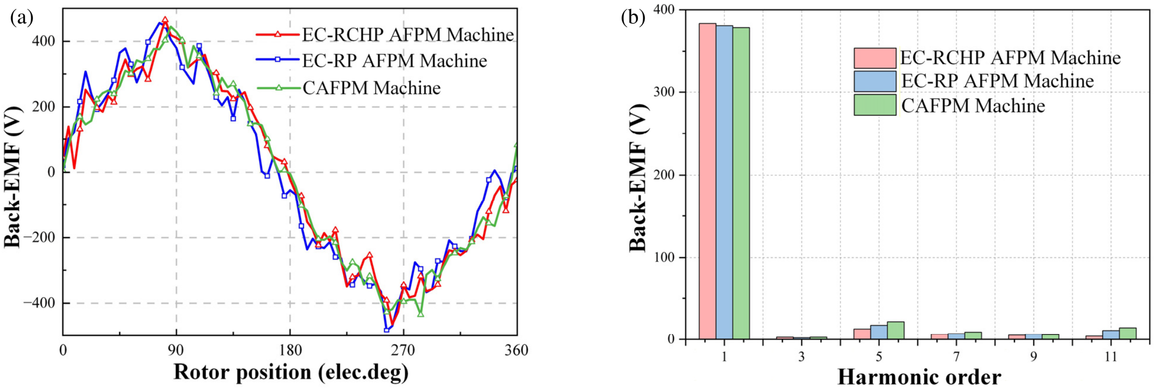

FIGURE 9. Analysis of open-circuit back EMF. (a) Back EMF waveforms at different rotor positions and (b) Fourier decomposition.

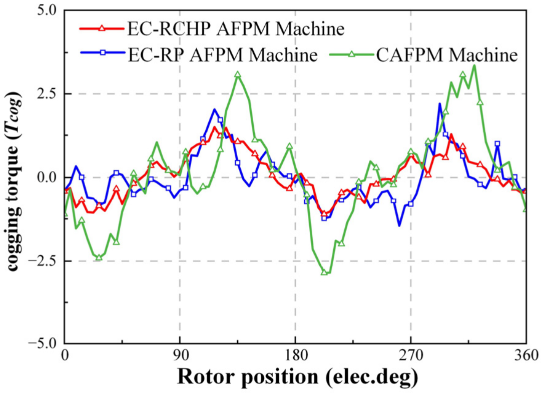

FIGURE 10. Analysis of the cogging torque characteristics of three machines.

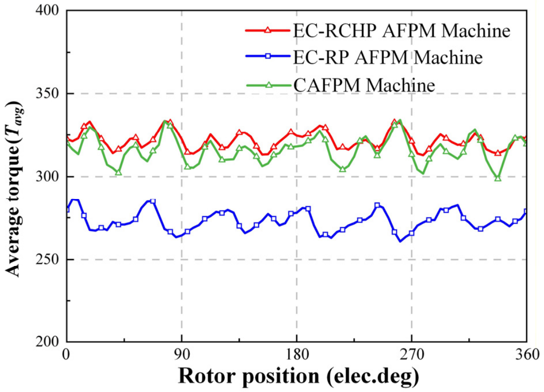

FIGURE 11. Analysis of the output torque characteristics of three machines.

The Fourier decomposition results in Figure 9(b) demonstrate that the back-EMF of the conventional CAFPM machine exhibits significant 5th and 7th harmonics. The total harmonic distortion (THD) values of the CAFPM, EC-RP AFPM, and EC-RCHP AFPM machines are 7.57%, 6.09%, and 4.25%, respectively. This confirms that the pole-shift technique effectively suppresses harmonic components through phase cancellation principle, thereby improving waveform quality and reducing the torque ripple and core losses of the machine.

4.3. Creep Torque Analysis

Cogging torque is an inherent characteristic of AFPM machines, and its peak magnitude directly governs vibration and noise levels, as well as the low-speed operational smoothness of the machine. Figure 10 compares the cogging torque waveforms of the three machines over a single electrical cycle. It can be observed from the waveforms that the maximum cogging torque of the CAFPM machine reaches 3.37 N·m. After applying the pole-shift technique, the maximum cogging torque of the EC-RP AFPM machine is reduced to 2.21 N·m, a decrease of 34.4%; that of the EC-RCHP AFPM machine is further reduced to 1.52 N·m, a remarkable reduction of 54.9%. These results confirm that the pole-shift technique effectively suppresses the peak cogging torque by introducing phase differences between the cogging torque components of different poles, which then cancel each other out.

4.4. Output Torque Characteristic Analysis

Figure 11 presents the output torque waveforms of the three machines under rated load conditions. Simulation results show that the CAFPM machine has an average output torque of 315.9 N·m and a torque ripple of 11.26%. After adopting the elliptical-cut pole-shift structure, the average torque of the EC-RP AFPM machine decreases to 273.0 N·m with a torque ripple of 6.12%. This demonstrates that although the pole-shift technique can reduce torque ripple, it inevitably leads to a moderate decrease in average torque. On this basis, the EC-RCHP AFPM machine incorporating the compensated Halbach array achieves an average torque of 321.7 N·m and a torque ripple of 6.12%. This validates the effectiveness of the proposed synergistic optimization scheme combining elliptical poles and Halbach arrays, which realizes high torque density while maintaining low torque ripple characteristics, making it well-suited to meet the application requirements of new energy vehicle drive motors for high power density and low vibration and noise.

5. CONCLUSIONS

To address the inherent limitation of conventional AFPM machines that cogging torque suppression and torque density enhancement cannot be simultaneously achieved, this paper proposes an EC-RCHP AFPM machine. The proposed machine is evaluated via FE analysis, leading to the following conclusions:

(1) By conducting equivalent surface current analysis on different machine topologies, this paper elucidates the fundamental mechanism by which elliptically skewed rotating poles suppress cogging torque, as well as the magnetic field enhancement mechanism of the compensated Halbach poles.

(2) Through the optimal design of Halbach auxiliary poles, the EC-RCHP AFPM machine not only further suppresses cogging torque but also fully compensates for the torque loss caused by the pole-shift technique, thereby successfully balancing high torque density and low torque ripple.

(3) Analysis of torque and back-EMF characteristics demonstrates that the EC-RCHP AFPM machine exhibits a more sinusoidal back-EMF waveform and lower THD, which is in good agreement with the theoretical analysis based on the equivalent surface current method. Furthermore, owing to the compensated Halbach pole design, the EC-RCHP AFPM machine achieves higher output torque and lower torque ripple than traditional CAFPM machines.

ACKNOWLEDGEMENT

This work was supported by the Postgraduate Innovation Special Fund of Jiangxi Province (No. YC2025-S589), in part by Jiangxi Provincial Postgraduate Innovation Special Fund Project (YC2025-B166).

REFERENCES

[1] Liu, X., H. Chen, J. Zhao, and A. Belahcen, "Research on the performances and parameters of interior PMSM used for electric vehicles," *IEEE Transactions on Industrial Electronics*, Vol. 63, No. 6, 3533–3545, Jun. 2016.

[2] Tu, R., H. Yang, H. Lin, H. Zhan, L. Chen, W. Chen, D. Wu, and M. Yu, "Electromagnetic-thermal coupled design of Halbach-array axial-flux PM machine for direct-drive automated guided vehicle," *IEEE Transactions on Transportation Electrification*, Vol. 11, No. 1, 2097–2107, Feb. 2025.

[3] Ming, G., L. Wu, L. Zhang, F. Niu, Y. Yan, Y. Fang, and Z. Zhu, "Comparative study of biased flux PM machines having different stator core segments and armature winding configurations," *IEEE Transactions on Transportation Electrification*, Vol. 8, No. 3, 3379–3389, Sep. 2022.

[4] Qu, H., Z. Q. Zhu, and B. Shuang, "Influences of PM number and shape of spoke array PM flux reversal machines," *IEEE Transactions on Energy Conversion*, Vol. 36, No. 2, 1131–1142, Jun. 2021.

[5] Lu, Y., J. Li, R. Qu, D. Ye, and H. Lu, "Electromagnetic force and vibration study on axial flux permanent magnet synchronous machines with dual three-phase windings," *IEEE Transactions on Industrial Electronics*, Vol. 67, No. 1, 115–125, Jan. 2020.

[6] Pranjić, F. and P. Virtič, "Cogging torque reduction techniques in axial flux permanent magnet machines: A review," *Energies*, Vol. 17, No. 5, 1089, 2024.

[7] Shi, X., G. Yu, and G. Li, "Experimental analysis on vibration and noise of motor bearing of washing machine," in *2021 4th World Conference on Mechanical Engineering and Intelligent Manufacturing (WCMEIM)*, 132–136, Shanghai, China, 2021.

[8] Lu, Z., Z. Xiang, X. Zhu, and M. Jiang, "Pole-slot combination design and investigation of spoke-type in-wheel motor considering flux modulation," in *2022 International Power Electronics Conference (IPEC-Himeji 2022-ECCE Asia)*, 2160–2166, Himeji, Japan, 2022.

[9] Shang, J., H. Zhang, T. Yao, M. Zhao, and D. Cheng, "A novel stator coreless disk motor with skewed wave winding for shaftless rim thruster," *IEEE Transactions on Applied Superconductivity*, Vol. 34, No. 8, 1–5, Nov. 2024.

[10] Zheng, M., Z. Q. Zhu, S. Cai, H. Y. Li, and Y. Liu, "Influence of stator and rotor pole number combinations on the electromagnetic performance of stator slot-opening PM hybrid-excited machine," *IEEE Transactions on Magnetics*, Vol. 55, No. 5, 1–10, May 2019.

[11] Wu, Z., W. Zhang, Z. Wang, L. Shao, W. Hua, and M. Cheng, "Stator semi-skewing method for high-speed permanent magnet machine," in *2025 28th International Conference on Electrical Machines and Systems (ICEMS)*, 693–697, Busan, Korea, 2025.

[12] Zhou, Y., W. Zhao, J. Ji, S. Zhu, and C. H. T. Lee, "Vibration mitigation in modular dual three-phase PMSM: Combined effects of winding topology and rotor skewing," *IEEE Transactions on Industrial Electronics*, Vol. 72, No. 12, 12 556–12 566, Dec. 2025.

[13] Yin, H., W. Hua, Z. Wu, and J. Du, "An efficient rotor-skewing model for mitigating electromagnetic vibration and noise in fractional-slot concentrated-winding permanent-magnet machines," *IEEE/ASME Transactions on Mechatronics*, Vol. 30, No. 2, 818–828, Apr. 2025.

[14] Zhou, Y., X. Wei, L. Yan, and X. He, "Hybrid analytical-numerical electromagnetic vibration calculation method for surface-inserted PMSMs with skewed slots," *IEEE Transactions on Energy Conversion*, Vol. 39, No. 4, 2654–2663, Dec. 2024.

[15] Ling, Z., W. Xu, W. Zhao, S. Meng, and M. Xu, "Design and analysis of a field modulated magnetic screw without permanent magnet skewing," *IEEE Transactions on Industrial Electronics*, Vol. 72, No. 9, 8798–8809, Sep. 2025.

[16] Zhang, Z., C. Wang, and W. Geng, "Design and optimization of Halbach-array PM rotor for high-speed axial-flux permanent magnet machine with ironless stator," *IEEE Transactions on Industrial Electronics*, Vol. 67, No. 9, 7269–7279, Sep. 2020.

[17] Yang, L., K. Yang, S. Sun, Y. Luo, F. Xiong, and C. Luo, "Study on the influence of a combined-Halbach array for the axial flux permanent magnet electrical machine with yokeless and segmented armature," *IEEE Transactions on Magnetics*, Vol. 60, No. 3, 1–5, Mar. 2024.

[18] Wang, A., X. Zhao, L. Liu, J. Cheng, H. Qiao, H. Wang, and J. Wang, "Design and analysis of the coaxial magnetic gears with Halbach PM arrays for downhole electric drilling tools," in *2023 26th International Conference on Electrical Machines and Systems (ICEMS)*, 3979–3983, Zhuhai, China, 2023.

[19] Hwang, S.-M., J.-B. Eom, G.-B. Hwang, W.-B. Jeong, and Y.-H. Jung, "Cogging torque and acoustic noise reduction in permanent magnet motors by teeth pairing," *IEEE Transactions on Magnetics*, Vol. 36, No. 5, 3144–3146, Sep. 2000.

[20] Zhou, R., G. Li, Q. Wang, J. He, and T. Wang, "Drive current calculation and analysis of permanent magnet spherical motor based on torque analytical model and particle swarm optimization," *IEEE Access*, Vol. 8, 54 722–54 729, Mar. 2020.

[21] Xue, Z., H. Li, Y. Zhou, N. Ren, and W. Wen, "Analytical prediction and optimization of cogging torque in surface-mounted permanent magnet machines with modified particle swarm optimization," *IEEE Transactions on Industrial Electronics*, Vol. 64, No. 12, 9795–9805, Dec. 2017.